Elsevier Editorial System(tm) for Medical Engineering & Physics

Manuscript Draft

Manuscript Number: MEP-D-04-00056R2

Title: Reduction of Compartment Compliance Increases Venous Flow Pulsatility and Lowers Apparent Vascular Compliance: Implications for Cerebral Blood Flow Hemodynamics

Article Type: Paper

Section/Category: Regular Issue Paper

Keywords: Intracranial pressure; Windkessel model; Apparent compliance

Corresponding Author: Dr. Xiao Hu, PhD

Corresponding Author's Institution: University of California, Los Angeles

First Author: Xiao Hu, Ph.D.

Order of Authors: Xiao Hu, Ph.D.; Abeer A Alwan, Ph.D.; Eduardo H Rubinstein, M.D., Ph.D; Marvin Bergsneider, M.D.

Manuscript Region of Origin:

Abstract: The global compliance of a fixed-volume, incompressible compartment may play a significant role in determining the inherent vascular compliance. For the intracranial compartment, we propose that the free-displacement of the cerebral spinal fluid (CSF) directly relates to cerebral vascular compliance. To test this hypothesis, an in vivo surrogate intracranial compartment was made by enclosing a rabbit's kidney within a rigid, fluid-filled container. Opening/closing a port atop the box modulated the free flow of box fluid (open-box state). We observed that the pulsatility of the renal venous outflow increased in response to hampering the free flow of fluid in-and-out of the container (closed-box state). To associate the observed pulsatility changes with the compliance changes, a parametric method was proposed for the computation of the apparent compliance (Capp) of the whole renal vascular system. The calculated Capp for each experiment's closed-

box state was favorably compared to a time-domain compliance assessment method at the mean heart rate. In addition, it was revealed that C_{app} in the open-box state was greater than that in the closed-box state only when the calculations were performed at frequencies lower than the heart rate and closer to the ventilation rate. These experimental results support the concept that the vessel compliance of vascular systems enclosed within a rigid compartment is a function of the global compartment compliance.

Reduction of Compartment Compliance Increases Venous Flow Pulsatility and Lowers Apparent Vascular Compliance: Implications for Cerebral Blood Flow Hemodynamics

Xiao Hu, Ph.D. [2,1]

Abeer A. Alwan, Ph.D.[3,2]

Eduardo H. Rubinstein, M.D., Ph.D.[4,5]

Marvin Bergsneider, M.D.[1,2]

[1]Division of Neurosurgery, [2]Biomedical Engineering Program, [3]Department of Electrical Engineering, [4]Department of Anesthesiology, [5]Department of Physiology. The David Geffen School of Medicine at UCLA. University of California, Los Angeles

Running Head: Apparent Compliance and Compartment Compliance

Corresponding Author: Marvin Bergsneider, M.D.

UCLA Division of Neurosurgery

10833 LeConte Ave.

74-134 CHS (Mail-Code 956901)

Los Angeles, CA 90095-6901

Office (310) 206-4100 FAX (310) 825-7245

email: mbergsneider@mednet.ucla.edu

ABSTRACT

The global compliance of a fixed-volume, incompressible compartment may play a significant role in determining the inherent vascular compliance. For the intracranial compartment, we propose that the free-displacement of the cerebral spinal fluid (CSF) directly relates to cerebral vascular compliance. To test this hypothesis, an *in vivo* surrogate intracranial compartment was made by enclosing a rabbit's kidney within a rigid, fluid-filled container. Opening/closing a port atop the box modulated the free flow of box fluid (open-box state). We observed that the pulsatility of the renal venous outflow increased in response to hampering the free flow of fluid in-and-out of the container (closed-box state). To associate the observed pulsatility changes with the compliance changes, a parametric method was proposed for the computation of the apparent compliance (C_{app}) of the whole renal vascular system. The calculated C_{app} for each experiment's closed-box state was favorably compared to a time-domain compliance assessment method at the mean heart rate. In addition, it was revealed that C_{app} in the open-box state was greater than that in the closed-box state only when the calculations were performed at frequencies lower than the heart rate and closer to the ventilation rate. These experimental results support the concept that the vessel compliance of vascular systems enclosed within a rigid compartment is a function of the global compartment compliance.

Keywords: Intracranial pressure, Windkessel model, Apparent compliance

INTRODUCTION

It has been demonstrated by magnetic resonance imaging [1, 2] that the pulsatile changes in intracranial arterial blood volume are intimately related to the dynamical movement of cerebrospinal fluid (CSF) across the foramen magnum. The rigid, fixed-volume enclosure of the skull establishes a common-compliance environment that links CSF hydraulic dynamics and cerebral hemodynamics [3, 4]. CSF compliance may be a key component of a "tuned" intracranial resonance system that is optimized for the lowest hemodynamic impedance [5, 6]. As a result, the pathological interference with the free movement of CSF, typically lowering CSF compliance, may hinder cerebral blood flow which, in turn, may result in any one in a number of intracranial pressure-related disorders (e.g. hydrocephalus).

The link between CSF movement and hemodynamic variables may have several mechanical avenues. In one proposed scenario [3], the intimate anatomic relationship between the major cerebral arteries and the subarachnoid space predicts that alterations in CSF compliance will have a direct influence on the arterial Windkessel function [7]. In the systemic circulation, the loss of arterial flow pulsatility principally occurs as a consequence of arterial vessel wall compliance [8]. However, within the rigid skull, the intracranial contents (brain, blood, and CSF) are nearly incompressible and therefore cerebral vascular compliance may be constrained by the global compartment compliance, which in turn, is primarily determined by the CSF system compliance. Under this scenario, a reduction in CSF compliance will cause a resulting loss of vascular compliance. Venous flow pulsatility, and hence total blood flow impedance, will subsequently increase.

In a second scenario, a reduction in CSF compliance would effectively improve the mechanical transmission of intracranial arterial pressures to the venous system [9]. Under such circumstances, presumably expansion of the arterial tree would cause a simultaneous compression of the venous system – thereby making the venous flow pulsatile.

In order to objectively ascertain whether a relationship between compartment compliance and venous pulsatility exists, we adapted a simple *in vivo* surrogate model of the intracranial compartment previously reported by Grande et al [10]. In this surrogate model, the brain and skull were conceptually substituted by a rabbit's kidney enclosed in an artificial rigid, watertight fluid-filled box. The displacement of fluid in and out-of the box, simulating the free flow of CSF across the foramen magnum, was controlled by a port atop the box.

Using the signals recorded from this experiment, we next sought to characterize how the changes in compartment compliance are associated with corresponding changes in vascular compliance. Because the latter could not be directly measured, we have developed a parametric method for estimating an apparent compliance (C_{app}). C_{app} was originally proposed by Quick et al [11] as a generalization of the classic 2-element Windkessel model without its unrealistic assumption of an infinite pulse wave velocity. We chose this methodology in the present work over the more traditional approaches of conducting parameter estimation for a lumped-parameter model to obtain compliance [12, 13].

METHODS

In Vivo Experiment Setup

The animal experiment protocols were approved by the UCLA Institutional Review Board overseeing animal research. The kidney of an adult New Zealand white rabbit was mobilized leaving the renal artery and vein anatomically and physiologically attached to the anesthetized (Halothane/Pancuronium) animal. The rabbits were induced using 5% inspired Halothane in 100% O_2 and maintained at 1.5-2% inspired Halothane in 100% O_2. The level of anesthesia was adjusted to maintain a steady level of heart rate and arterial pressure. Mean expiratory halothane (and CO_2) concentration was continuously monitored using a clinical anesthetic monitoring unit. In addition, EEG was continuously monitored for depth of anesthesia. The kidney was positioned in a custom-made acrylic container that had an opening to accommodate the renal vessels in a watertight manner. Cyanoacrylate glue was used to both maintain the vessel wall geometry and provide the watertight seal across the container opening. The container, designed just large enough to accommodate the kidney, was completely filled with 0.9% NaCl saline solution. The compliance of the container was controlled by a port (4 mm internal diameter) located on top of box, which could be occluded to make the container a closed system. Renal arterial and venous flow patterns were continuously monitored by circumferential 20-MHz gated Doppler ultrasound probes positioned on the vessels immediately outside the container. Systemic arterial blood pressure was measured using a 20-G catheter placed in either the femoral or common carotid artery and fluid coupled to a pressure transducer. Container pressure was measured via a separate box port connected to a fluid coupled transducer.

The box fluid temperature was maintained at 38 °C using a thermocouple controlled heating lamp.

Fig. 1 illustrates the experimental setup and measurement sites. The following signals were measured: arterial blood pressure (P_a); renal arterial flow at the entrance of the container (Q_a); renal venous flow at the outlet of the container (Q_v); container fluid pressure (P_b).

The signals were collected via a multichannel PowerLab/16SP data acquisition system sampled at 100 Hz. The data from five separate animal experiments was analyzed. Measurements were taken with the port atop the box open (open box state) or occluded (closed box state). A fifteen-second stable epoch was extracted for processing for each box state. Each epoch was low-pass filtered using a zero-phase elliptic infinite impulse response filter. Zero phase was achieved using the two-pass schema introduced in [14]. The filter was designed with a cut-off frequency at 8 Hz. Since the heart rate was in the range of 4.0~5.0Hz, this low pass filter essentially removed all the harmonic components of heart rate except the fundamental one.

Parametric Computation of Apparent Compliance

C_{app} was originally defined as a transfer function (TF) between the volume (V_s) stored in the target vascular bed and the pressure (P_i) at its entrance [11]. Based on the principle of conservation of mass, the volume stored equals the integration of the difference between inflow and outflow. Expressed in the Fourier transform (FT) domain:

$$V_s(\omega) = \frac{1}{j\omega}\left[Q_i(\omega) - Q_o(\omega)\right] \quad (1)$$

where $V_s(\omega)$, $Q_i(\omega)$, and $Q_o(\omega)$ are FT of $V_s(t)$, $Q_i(t)$, and $Q_o(t)$ respectively. Given the above equation, C_{app} can be represented as:

$$C_{app}(\omega) = \frac{1}{j\omega} \frac{[Q_i(\omega) - Q_o(\omega)]}{P_i(\omega)} \tag{2}$$

where $j = \sqrt{-1}$ and $P_i(\omega)$ is the FT of inlet pressure. This definition of C_{app} reconciles the classical Windkessel model and the more realistic transmission line model of vascular systems [11].

A parametric system identification was used for estimating TF and hence C_{app} based on the advantage that it only prescribes a linear relationship between the input and output of the system without regard to how the internal states of the system evolve. This also frees it from the unrealistic assumption of infinite pulse wave velocity in traditional lumped models. An additional benefit is that number of samples used for identifying a parametric model usually dominates the number of unknown parameters. This improves the quality of the estimate compared to a non-parametric approach where the number of data samples equals the number of unknowns. Finally, there is no limitation on frequency resolution as imposed by the length of signals.

Of the various available forms of parametric models, the autoregressive model with exogenous input (ARX) was chosen here. An advantage of ARX model stems from the fact that its unknown parameters can be obtained by solving a linear least squares problem while more complicated approaches have to be taken for other models (such as state-space models).

ARX is a popular input-output model suitable for modeling a linear discrete dynamic system that relates an output signal (y) to an input signal (u). In the present context,

output signal is considered as $Q_i - Q_o$, i.e., the differential arteriovenous blood flow signal, and input signal as P_i. In time domain, the following relationship between y and u is assumed:

$$y(n) = -\sum_{i=1}^{N_y} a_i y(n-i) + \sum_{k=0}^{N_u-1} b_k u(n-k) + e(n) \tag{3}$$

where a_i and b_k are model coefficients. It basically assumes that the current sample of y is a linear weighted summation of its N_y previous samples plus the linear weighted summation of N_u input samples. The model error is lumped into the error signal $e(n)$.

The corresponding transfer function for an ARX model can be analytically calculated (for any frequency ω)

$$H(\omega) = \frac{\sum_{k=0}^{N_u-1} b_k \exp(-j\omega k)}{1 + \sum_{i=1}^{N_y} a_i \exp(-j\omega i)} \tag{4}$$

Unknown parameters a_i and b_k were identified in an off-line fashion based on N samples of u and y using the standard least squares approach [15]. There is no prior knowledge regarding the appropriate values that N_u and N_y should be for the system studied here. Generally, with increasing N_u and N_y, the fitting of the model to a particular pair of u and y will become better. However, excessively large N_u and N_y will compromise the capability of the identified model to represent the true dynamics of the system and thus should be avoided. The principle of Minimum Description Length (MDL) is used for determining an appropriate set of N_u and N_y that balance the number of parameters with the goodness of fit. Let p denote the total number of model

parameters, i.e., $(N_u + N_y)$ and N the total number of samples used for fitting the model, MDL criterion can be calculated as:

$$MDL(p) = N\log\left(\frac{V(p)}{N}\right) + \log(N)p \tag{5}$$

where $V(p)$ is the squared fit error of the model at a particular combination of N_u and N_y. Based on MDL, the optimal p was selected as the one that achieved the minimal MDL among a given set of N_y and N_u combinations.

With the calculated $H(\omega)$, $C_{app}(\omega)$ can be easily calculated according to Eq. 2)

$$C_{app}(\omega) = \frac{H(\omega)}{j\omega} \tag{6}$$

Determination of Variance of the Apparent Compliance

Apparent compliance is determined from the measured data without any prior information about its true value. Equation 6 gives such an estimate but lacks the information regarding how good one estimate is. Bias and variance of an estimate are two important quality indicators. From the parametric spectral estimation theory [16], we know that an apparent compliance estimate given by Eq. 6 is asymptotically consistent meaning that bias approaches zero with increasing number of samples for estimation. With this result established, only its variance needs to be assessed to complement Eq. 6. Furthermore, given that we are only interested at $|C_{app}(\omega)|$, i.e., the magnitude of the apparent compliance, we only calculate the variance of $|C_{app}(\omega)|$.

The stochastic effect due to the inaccuracy of the chosen ARX model as well as the measurement noise is lumped into the white noise sequence in Eq. 3. This in consequence turns the identified ARX model coefficients, i.e., a_i and b_k into random variables

having a covariance matrix $C_{(N_u+N_y)\times(N_u+N_y)}$, which can be obtained from the process of fitting ARX. Given the fact that $\left|C_{app}(\omega)\right|$ is a nontrivial function of random variables a_i and b_k, an accurate derivation of is variance is a formidable task if not impossible. To proceed as a usual practice in parametric spectral estimation, the following quantity will be used as an approximation of the variance of $\left|C_{app}(\omega)\right|$

$$\mathrm{var}\left(\left|C_{app}(\omega)\right|\right) \approx J(\omega)^T C J(\omega) \tag{7}$$

where $J(\omega)$ is the gradient (a column vector) of $\left|C_{app}(\omega)\right|$ with respect to a_i and b_k evaluated at their estimated values. More details about the above approximation's underlying derivation can be found in [17]. Based on Eqs. 4 and 6, evaluation of the gradient results in:

$$\frac{\partial\left|C_{app}(\omega)\right|}{\partial b_i} = \frac{\mathrm{Re}\left[\exp(-j\omega i)\sum_{k=0}^{N_u-1} b_k \exp(-j\omega k)\right]}{\omega\left|H(\omega)\right|\left|\sum_{k=1}^{N_y} a_k \exp(-j\omega k)\right|},\ i=0,\cdots,N_u-1 \tag{8}$$

and

$$\frac{\partial\left|C_{app}(\omega)\right|}{\partial a_i} = \frac{\left|H(\omega)\right|}{\omega\left|\sum_{k=1}^{N_y} a_k \exp(j\omega(i-k))\right|}\mathrm{Re}\left[\sum_{k=1}^{N_y} a_k \exp(j\omega(i-k))\right],\ i=1,\cdots,N_y \tag{9}$$

where $\mathrm{Re}[x]$ operator returns the real part of a complex variable x.

Hence, variance of $\left|C_{app}(\omega)\right|$ can be calculated

$$Var\left(C_{app}(\omega)\right)=\left[\frac{\partial\left|C_{app}(\omega)\right|}{\partial a_i}\quad\cdots\quad\frac{\partial\left|C_{app}(\omega)\right|}{\partial b_k}\quad\cdots\right]\begin{bmatrix}\Sigma_a & \Sigma_{a,b}\\ \Sigma_{b,a} & \Sigma_b\end{bmatrix}\left[\frac{\partial\left|C_{app}(\omega)\right|}{\partial a_i}\quad\cdots\quad\frac{\partial\left|C_{app}(\omega)\right|}{\partial b_k}\quad\cdots\right]^T \tag{10}$$

where the covariance matrix C is illustrated in a decomposed form such that the (i,j) element of Σ_a is the covariance of coefficients a_i and a_j.

Test of Zero Coherence

From the perspective of experimental design for system identification, the benefits of adopting a "white" stimulating signal to the system to be identified has long been realized. In the cardiovascular research, random perturbation of the heart rate, if permissible, has been the established way of achieving this effect. In situations where no such endeavor has been done as in the present experiments, a remedy is to check for the zero coherence of the input and output signals at the interested frequencies via computing the squared coherence spectrum as following:

$$\gamma^2(\omega)=\frac{\left|P_{x,y}(\omega)\right|^2}{P_x(\omega)P_y(\omega)} \tag{11}$$

where $P_x(\omega)$ and $P_y(\omega)$ are the power spectral densities of input signal x and output signal y respectively and $P_{x,y}(\omega)$ is the cross-power spectral density between them. Many researchers have realized the importance of checking coherence for obtaining reliable results. However, most of them have chosen one hard threshold for rejecting low-coherent points. A rigorous statistical test actually exits for testing zero coherence based on the non-parametric spectral analysis [17]. A brief description of this test is given here.

Under the hypothesis that coherence is zero, the frequency dependent statistic $(\nu-2)\gamma^2(\omega) \Big/ \left[2-2\gamma^2(\omega)\right]$'s distribution is $F_{2,\nu-2}$. ν is defined as an equivalent degree of freedom, which is calculated, according to [18], as

$$\nu = \frac{2\mathrm{K}}{1+\sum_{\mathrm{i}=1}^{K-1}\beta(i) - \frac{1}{K}\sum_{\mathrm{i}=1}^{K-1} i\beta(i)} \tag{12}$$

Where $\beta(i) = \left[\sum_{k=0}^{L-1-i\tau} w(k)w(k+i\tau) \Big/ \sum_{k=0}^{L-1} w^2(k)\right]^2$, $w(k)$ is the data taper function (chosen to be the standard Hanning window here) for smoothing the signal, L is the window length and τ is the step of moving window and K is the number of L-sample segments as determined by the given L, τ and the total signal sample length. Thus by defining a confidence level (0.95 used here), one can calculate the threshold δ to test whether $\gamma^2(\omega)$ is zero or not. δ can be derived as:

$$\delta = \frac{2F_{2,\nu-2}}{\nu - 2 + 2F_{2,\nu-2}} \tag{13}$$

Assessment of Compliance Based on Pulse Waves

In the closed-box situation, the whole system must maintain an isovolumeric state with each heart-beat. Therefore any increase or decrease in volume due to the instantaneous difference between the inflow and outflow of the system should be compensated by the compliance of the system. Using a beat-to-beat analysis of the container pressure, the inflow, and outflow signals, one can reconstruct a volume-pressure curve for each heart-beat and obtain the associated compliance as the derivative of this curve based on the physical definition of the compliance. Following this

reasoning, the time-domain estimation of compliance C_{pulse} can be calculated for each heart beat. Its average over the whole signal segment was then used as a global representation of compliance of the system. Another advantage of this approach of assessing compliance is the avoidance of manually injecting fluid into the container. Several trials of that approach have been attempted with a very low success rate of keeping the system from leaking during the fluid infusion. Conceptually, C_{pulse} should correspond to the apparent compliance (C_{app}) at the heart-rate and thus obtaining C_{pulse} facilitates a validation of the C_{app}. An illustration of calculating C_{pulse} for a single heart beat is illustrated in Fig. 2. In Panel A, a cycle of container pressure P_b is displayed in the upper plot together with its corresponding $Q_a - Q_v$ in the lower plot. Data points having a positive slope on P_b and being positive on the corresponding $Q_a - Q_v$ are marked with circles. Those points also correspond to the increasing branch of the Pressure-Volume curve derived from P_b and $Q_a - Q_v$ shown in Panel B. C_{pulse} can then be calculated as the slope of this portion of the curve of the Pressure-Volume indicating that net inflow caused an increase in P_b. Similarly, one can identify the decreasing branch of the Pressure-Volume curve, which corresponds to a net outflow condition to calculate C_{pulse}. It has been verified in the present work that C_{pulse} derived from these two branches did not show significant difference. Hence, C_{pulse} calculated using the net inflow Pressure-Volume curve was reported here.

RESULTS

Figure 3 shows representative plots of the four recorded signals with an abrupt transition from an open-box state to a closed-box state transition. The open-box venous flow pulsatility was very low. Immediately upon closing the port atop the box, an increase in the venous flow as well as the container fluid pressure pulsatilities was clearly visible while there were no changes in arterial pressure and arterial flow. A summary of mean and pulsatility for each signal and for each port state is given in Table 1. Pulsatility was calculated, for each cycle, as the amplitude of the first harmonic of a signal. A two-sample two-tailed student *t* test was applied for testing if there is a significant ($p<0.01$) difference between mean values of signals at open and closed box states. On the other hand, a one-tailed test was applied for pulsatility with the hypothesis that closing box increased pulsatility. Those pairs with significant outcomes are marked with "*" in the table cells between them. A significant increase of pulsatility of both container fluid pressure and venous outflow is evident in the table. Mean values of container fluid pressure also changed. There are two cases where mean arterial pressure and arterial flow showed a significant change.

The instantaneous net volume change of the system in the closed-box state was estimated by integrating the difference between arterial inflow and venous outflow. This instantaneous volume change signal, plotted together with P_a and P_b in Fig. 4, demonstrates a phase lag between P_a and the volume signal. This lag presumably was caused by the finite pulse wave velocity. Its existence suggests the appropriateness of adopting the apparent compliance approach. In addition, it is observed that P_b was more

in phase with the volume signal, indicating an infinite pulse wave velocity for the pressure wave transmission across the box fluid.

A plot of $|C_{app}(\omega)|$ versus frequency is illustrated in Fig. 5 for each experiment. $|C_{app}|$ is shown for frequencies ≤ 1.2 times the mean heart rate with a resolution of 0.1 Hz. Coherent points are marked on each curve. There are two main coherent regions: one high frequency part around heart rate and one low frequency region possibly around respiratory frequency. Figure 5 shows that the difference between the open-box and closed-box $|C_{app}|$ decreases as frequency increases. The open-box $|C_{app}|$ is higher than that of the closed-box $|C_{app}|$ within the frequency range studied.

The phase characteristics of C_{app} is presented in Fig. 6. The phase of C_{app} does not approach zero as frequency decreases to zero. This may have resulted from incorporating the compliant venous system into the apparent compliance calculation. For illustrative purpose, the spectra of squared coherency for each experiment are displayed in Fig. 7 with the zero threshold plotted as a straight line. Threshold was calculated using Eq. 13.

Table 2 summarizes the heart rate and optimal ARX model order resulted from the MDL criterion for each signal epoch processed. A t-test indicates that heart rate was not significantly different between two port states. There are three pairs of signal epochs that have the same ARX model orders (both N_u and N_y) even though their $|C_{app}(\omega)|$ spectra shows similar pattern as the remaining two that have different N_y. This indicates

that different model orders for open and closed box state are not responsible for different $|C_{app}(\omega)|$ at these two different states.

Table 3 summarizes $|C_{app}|$ and C_{pulse} calculated at the fundamental heart-rate frequency. The mean and standard deviation of C_{pulse} were pooled from individual ones calculated for each heart-beat. The ratio of $|C_{app}|$ to mean C_{pulse} indicates that they are essentially in the same order of magnitude.

Figure 8 shows the phase spectra of Q_a, Q_v, and P_b relative to the common reference signal P_a. Similar to Figs. 5 and 6, coherent points common to all three signals are marked with different symbols for each signal respectively. In all experiments, Q_a led both Q_v and P_b. Q_v nearly always led P_b at lower frequencies. On the other hand, Q_v phase relationship to P_b revealed two patterns around the heart rate. The phase spectra of experiments No. 1, 2 and 4 showed that Q_v lagged P_b while Q_v and P_b were more in phase for experiments No. 3 and 5. The coexistence of these two patterns may provide insights to the functioning of two pulse transmission routes from the arterial to the venous circulation as depicted in Fig. 9, which will be addressed in detail in the following Discussion section.

DISCUSSION

The strict definition of compliance of an isolated vascular bed is only associated with the mechanical distensibility and the geometric size of the vessels. It determines how the pressure in that vascular system will respond to volume changes. In an *in vivo*

situation, the volume and pressure relationship is also subject to the effects of tissues surrounding the vascular bed, the wave transmission and reflection phenomenon, and in our case compartmental fluid translocation. All these factors lumped together can lead to a complex pressure-volume relationship. A proper interpretation of the various terms used in the text such as CSF system compliance and global compartment compliance can only be achieved with this *in vivo* consideration and hence validates our choice of using apparent compliance for the quantitative analysis.

The results of the present work suggest that a reduction in the peri-vascular compliance causes a dramatic increase in venous flow pulsatility. Furthermore, apparent compliance is able to quantify the effect caused by blocking container fluid flow on the measured hemodynamic signals. The parametric $|C_{app}|$ estimation method can provide meaningful results as verified by a more direct assessment method. The formula for calculating the variance of parametric $|C_{app}|$ complements the proposed C_{app} estimation method.

The difference between the open-box $|C_{app}|$ and the closed-box one was the greatest at the lower frequencies and $|C_{app}|$ is also higher at the lower frequencies. These results may be a consequence of the changes in organ blood volume as a function of the respiration. During mechanical ventilation, the inspiratory pressure increases as well as the central venous pressure. The latter change also elevates the renal venous pressure and augments the organ blood content. Conversely, during expiration, renal venous pressure decreases and consequently the intrarenal blood volume decreases. This cyclic alternation of the organ blood content occurs at the respiratory rate and has been reflected in the

calculation of apparent compliance, with a relatively high value in the open box situation. One necessary condition for this to take place would be to have a high compliance in the vascular bed, primarily on the venous side. Interestingly, during the closed box situation, the respiratory variation in renal blood volume did not occur, because the distensibility of the vascular bed was reduced (because of the failure in the translocation of the fluid in the box). In this situation, the apparent compliance was reduced. Hence, it is possible that the estimation of the apparent compliance does not have the sensitivity to pick up the small changes in blood volume that follow each systolic pulse while it may reflect the alteration in renal blood volume that results from the respiratory variations in renal venous pressure.

Apparent compliance, as a black-box approach, does not provide information regarding what causes the compliance changes. We have considered two routes by which the incoming arterial pulse wave can be transmitted to the renal veins in a closed-box state. As graphically depicted in Fig. 9, there is a vascular transmission route via renal vascular bed (panel B) versus a "short-circuit" arterial-venous transmission via the box fluid (panel C). Functioning of these two routes can cause similar changes in an apparent compliance spectrum. However, they should result in different phase relationship among Q_a, Q_v, and P_b with regard to P_a. Specifically, if the "short-circuit" route dominated, P_b and Q_v will be more in phase than the situation where vascular transmission route was functioning. Based on our analysis of the phase relationships between Q_a, Q_v, and P_b (Fig. 8), it is likely that both scenarios may be functioning in a closed-box state but at different relative proportions (perhaps due to small unknown differences in the experimental setup across animals). In addition, both appear to be disabled in the open-

box state (panel A) where the direct route was diverted to the opening atop the box and the pulse wave through the vascular route filtered out by the vascular compliance. Our results showedd that mean container pressure was almost always higher in the closed box state than in the open box one. Given the collapsible nature of the renal veins and the increased container pressure, a so called "vascular waterfall" phenomenon [19] may occur, in which case changes of the downstream venous blood flow would not be influenced by the changes of the pressure drop from renal capillary bed to the veins, an equivalent cutoff of the vascular transmission route for flow pulse wave. Since no venous pressure was measured and neither the critical closing pressure of renal veins, the question regarding whether or not the vascular waterfall happened cannot be clearly ascertained. In addition, due to the *in vivo* nature of our experimental setup, the venues blood flow did not empty to open air and hence further complicates the ideal situation for vascular waterfall phenomenon.

Modeling compliance appropriately has been the key of any lumped-parameter model of intracranial dynamics. The prevailing structure concerning the arrangement of vascular compliance and brain tissue compliance as adopted in various models [20-22] is to link vascular compliance with brain tissue compliance via a common node where node pressure is taken as intracranial pressure. This arrangement essentially models the fixed-volume constraint for the whole intracranial system and the results in the present work are supportive of this modeling practice by showing that apparent compliance as derived purely from hemodynamic variables can be changed by compartment compliance.

Our experimental model was intended to be a simplified analogue of the intracranial compartment. We speculated that as intracranial compliance decreases, the

vascular compliance would become constrained and therefore defined by the global intracranial compliance. There are multiple mechanisms by which intracranial compliance can become impaired pathologically, including the obstruction of the dynamical flow of CSF across the foramen magnum. In such a pathological situation, we have hypothesized that the intracranial arterial system changes to a "rigid-tube" system. Because the Windkessel is impaired, the low-pass filtering effect will be reduced and therefore the pulsatile arterial flow pattern will be maintained throughout the intracranial vascular system.

Changes in intracranial venous pulsatility have been documented clinically with varying intracranial compliance states. Carmelo et al [9] measured superior sagittal sinus velocity waveforms in patients in whom a large decompressive craniectomy had been performed. They noted no apparent pulsatility in the blood flow velocity. Following a cranioplasty for replacement of the skull defect, venous pulsatility returned. The results of their clinical study nearly parallel those of our *in vivo* experiment, although our interpretations differ somewhat. Based on the phase lag between the carotid pulse and the venous flow peak (in the closed-cranium situation), Carmelo et al. concluded that the direct arterial-to-venous pressure transmission was operative. Our phase analysis supports the conclusion of this clinical study but also suggests that transvascular ("rigid-tube") may be at play as well, perhaps at more pathological extremes.

Based on some published literature, one might question whether there is a demonstrable Windkessel effect occurring within the intracranial compartment. It has been suggested that the cerebral circulation exhibits primarily high-pass filter characteristics, leading to a reduction of only the DC component of cerebral blood flow

[23]. This study, however, was limited to inferences made based on Doppler data obtained from the extracranial internal carotid artery only. Because blood flow pulsations in the cerebral capillaries have not been directly measured[24], it has been difficult to definitively assess the efficiency of the intracranial Windkessel. A study of "cortical flow" using the laser Doppler techniques did indicate pulsatility in capillaries[25].

Intracranial venous outflow patterns, however, have been directly measured. Greitz [1], using gated magnetic resonance imaging, demonstrated that the blood flow velocity in the superior sagittal sinus did indeed exhibit a phase shift and smoothing compared to that measured in the carotid siphon – a finding consistent with low-pass filtering. A similar representation was reported in [26].

Our experimental model, of a kidney enclosed in a saline filled acrylic container, was intended to be a first order approximation of the intracranial compartment. This model, like that of Grande et al. [10], has the advantage of studying a complex phenomenon with a relatively simple setup. In addition to being anatomically accessible, the kidney shares many important traits with the brain. Both demand a high proportion of the total cardiac output and actively auto-regulate. There are important differences, however, that we could not measure nor assess. It is believed that the cerebral arteries have much less elastin in the media and adventitia, but more prominent internal elastic lamina than the arteries of extracranial sites[27]. Another limitation of the model is attributed to the fact that renal tissue pressure was not measured, which could have been more appropriate for surrogating intracranial pressure than the fluid pressure inside the box. Block of cerebrospinal fluid pathway was simulated by a complete closure of a port atop the box, which apparently could not model a chronic or partial CSF pathway

blockage. With these limitations in mind, the generalization of this animal model should be cautious and should be within the intended scope of the study, i.e., the relationship between the compliance and the observed venous flow pulsatility. Given the robust changes in flow pulsatility seen in our experiment, the model is valid for studying this phenomenon.

Blood flow autoregulation is a phenomenal manifestation of various flow control mechanisms of heterogeneous origins, time scales and time delays. No effort has been made to block any renal flow control route during the experiment. Hence autoregulation could potentially confound the apparent compliance spectrum since vessel radii alternations change vascular compliance and resistance. This confounding is expected to happen at the lower end of the spectrum. Hence, apparent compliance, being a transfer function analysis of pressure and volume signals provides a new conceptual way of studying autoregulation in addition to the existing approach of transfer function analysis of pressure and flow (flow velocity) signals.

The results of this relatively simple *in vivo* experiment support the concept that changes in the perivascular environment, specifically a reduction in compliance, produce significant changes in venous flow hemodynamics. Our modeling efforts further support our hypothesis that vascular compliance, depicted as C_{app}, changes with compartment compliance. Further experimental work will be necessary to validate whether C_{app} can be used clinically.

Acknowledgement

This work was supported by NINDS RO1 NS40122-01. We wish to thank the contribution of Lisa Falkson, M.S.

REFERENCES

[1] Greitz D. Cerebrospinal fluid circulation and associated intracranial dynamics. A radiologic investigation using MR imaging and radionuclide cisternography. Acta Radiol Suppl.1993;386:1-23.

[2] Greitz D, Franck A, and Nordell B. On the pulsatile nature of intracranial and spinal CSF-circulation demonstrated by MR imaging. Acta Radiol.1993;34:321-8.

[3] Bergsneider M, Alwan AA, Falkson L, and Rubinstein EH. The relationship of pulsatile cerebrospinal fluid flow to cerebral blood flow and intracranial pressure: a new theoretical model. Acta Neurochir Suppl (Wien).1998;71:266-8.

[4] Bergsneider M. Evolving concepts of cerebrospinal fluid physiology. Neurosurg Clin N Am.2001;12:631-8, vii.

[5] Egnor M, Rosiello A, and Zheng L. A model of intracranial pulsations. Pediatr Neurosurg.2001;35:284-98.

[6] Egnor M, Zheng L, Rosiello A, Gutman F, and Davis R. A model of pulsations in communicating hydrocephalus. Pediatr Neurosurg.2002;36:281-303.

[7] Frank O. Die Grundform des Arteriellen Pulse. Z.Biol.1899;37:483-526.

[8] Yin F, and Z.Liu., Arterial compliance-physiological viewpoint, in In:Vascular Dynamics. Physiological Perspectives, N. W. a. D.R.Gross, Ed. New York: Plenum, 1989.

[9] Carmelo A, Ficola A, Fravolini ML, La Cava M, Maira G, Mangiola A, and Marchese E. ICP and CBF regulation: effect of the decompressive craniectomy. Acta Neurochir Suppl.2002;81:109-11.

[10] Grande PO, Asgeirsson B, and Nordstrom CH. Physiologic principles for volume regulation of a tissue enclosed in a rigid shell with application to the injured brain. J Trauma.1997;42(5 Suppl):S23-31.

[11] Quick CM, Berger DS, and Noordergraaf A. Apparent arterial compliance. Am J Physiol.1998;274(4 Pt 2):H1393-403.

[12] Cappello A, Gnudi G, and Lamberti C. Identification of the three-element windkessel model incorporating a pressure-dependent compliance. Ann Biomed Eng.1995;23:164-77.

[13] Shim Y, Pasipoularides A, Straley CA, Hampton TG, Soto PF, Owen CH, Davis JW, and Glower DD. Arterial windkessel parameter estimation: a new time-domain method. Ann Biomed Eng.1994;22:66-77.

[14] Kormylo JJ and Jain VK. Two-pass recursive digital filter with zero phase shift. IEEE Transactions on Acoustics, Speech, & Signal Processing.1974;ASSP-22:384-7.

[15] Ljung L. 'System identification : theory for the user', 2nd ed. Upper Saddle River, NJ: Prentice Hall PTR, 1999.

[16] Kay SM. 'Modern spectral estimation : theory and application'. Englewood Cliffs, N.J.: Prentice Hall, 1988.

[17] Priestley MB. 'Spectral analysis and time series'. London ; New York: Academic Press, 1981.

[18] Welch PD. The Use of Fast Fourier Transform for the Estimation of Power Spectra: A Method Based on Time Averaging Over Short Modified

Periodograms. IEEE Transactions on Audio and Electroacoustics.1967;AU-15:70-73.

[19] Permutt S and Riley RL. Hemodynamics of Collapsible Vessels with Tone: The Vascular Waterfall. J Appl Physiol.1963;18:924-32.

[20] Agarwal GC, Berman BM, and Stark L. A lumped parameter model of the cerebrospinal fluid system. IEEE Trans Biomed Eng.1969;16:45-53.

[21] Ursino M. A mathematical study of human intracranial hydrodynamics. I. The cerebrospinal fluid pulse pressure. Annals of Biomedical Engineering.1988;16:379-401.

[22] Ursino M and Giammarco PD. A mathematical model of the relationship between cerebral blood volume and intracranial pressure changes: the generation of plateau waves. Annals of Biomedical Engineering.1991;19:15-42.

[23] Michel E HS, vonTwickel J, Zernikow B, Jorch G. Frequency dependence of cerebrovascular impedance in preterm neonates: a different view on critical closing pressure. J Cereb Blood Flow Metab.1997;17(10):1127-31.

[24] Kadas ZM, Lakin WD, Yu J, and Penar PL. A mathematical model of the intracranial system including autoregulation. Neurol Res.1997;19:441-50.

[25] Curran-Everett D ZY, Jones RH, Jones MD Jr. Hypoxia, hypercapnia, and hypertension: their effects on pulsatile cerebral blood flow. J Appl Physiol.1995;79:870-8.

[26] Avezaat CJ and van Eijndhoven JH. Clinical observations on the relationship between cerebrospinal fluid pulse pressure and intracranial pressure. Acta Neurochir (Wien).1986;79:13-29.

[27] Nagasawa S, Handa H, Okumura A, Naruo Y, Okamoto S, Moritake K, and Hayashi K. Mechanical properties of human cerebral arteries: Part 2. Vasospasm. Surg Neurol.1980;14:285-90.

FIGURE LEGENDS

Figure 1. A schematic plot of the experiment setup. P_a is the arterial blood pressure. Q_a is the renal arterial flow measured at the entrance of the container and Q_v the renal venous flow at the outlet of the container. P_b is the container fluid pressure.

Figure 2. An illustration of calculating C_{pulse}. In panel A, upper plot gives a cycle of P_b and lower plot displays the corresponding $Q_a - Q_v$. Points marked on the P_b and $Q_a - Q_v$ curves are those with a positive slope on P_b and positive value on $Q_a - Q_v$. The corresponding pressure-volume curve is displayed in the lower panel. C_{pulse} is estimated as the slope of the marked portion of pressure-volume curve that can viewed as a pressure-volume curve from the injection of blood by a pulse into the system.

Figure 3. Plot of the four signals recorded at a representative experiment. The sample corresponding to the location of the annotated port-closing event is marked with a circle.

Figure 4. Overlaid plot of the normalized unitless container fluid pressure, arterial pressure, and net volume change of the system for the closed-box state. All signals were normalized to be within $[-1,1]$ for a better illustration of their phase relationships. The existence of a lag between P_a and the net volume change supports the application of apparent compliance for its independence from the assumption of an infinite pulse wave speed as compared to the traditional Windkessel model.

Figure 5. Amplitude of apparent compliance for five selected records. The five amplitude curves are similar in shape and the apparent compliance in the open-box state is larger than that of the closed-box state. As mentioned in the text, points on $|C_{app}|$ curve that have a significant non-zero coherency are marked with 'o' and '*' for the closed-box and the open-box state, respectively.

Figure 6. Phase of apparent compliance for five selected records. Phase curves of experiments 1, 3 and 5 are similar in shape while those of experiments 2 and 5 are close to each other. Similar to Fig. 5, coherent points are marked on the curves.

Figure 7. Squared coherency $\gamma^2(\omega)$ between P_a and $Q_a - Q_v$. For each plot, a straight line equaling the threshold for detecting zero coherency is plotted. Spectrum points having a coherency above the threshold are marked in the reported apparent compliance spectrum in Figs. 5 and 6.

Figure 8. Phase spectra of the five experiments for arterial inflow, venous outflow, and container fluid pressure. All are calculated relative to arterial pressure. Similar to Figs. 5 and 6, coherent points are marked with different symbol on each curve. The frequency corresponding to the mean heart rate of signals is marked with a star symbol.

Figure 9. A graphic representation of two possible pulse wave transmission routes in the closed-box states. They include: a vascular route through the renal vascular bed due to

the loss of Windkessel effect (as shown on panel B) and a shortcut through the box fluid (as shown on panel C). The appearance of the pulsatile venous blood flow could be due to the combined effects of both in the closed box state. In the open box state (panel A), both appear to be disabled where the direct route was diverted to the opening atop the box and the pulse wave through the vascular route was filtered out by the vascular compliance.

TABLE CAPTIONS

Table 1. A summary of mean (M) and pulsatility (P) of four signals including arterial pressure, arterial flow, container pressure and venous flow at open (O) and closed (C) states. Data are presented in terms of its mean value and standard deviation pooled from all heart beats processed. Pulsatility was calculated as the amplitude of the first harmonic of a signal. A two-sample student *t* test was applied to test if there was a significant difference between two box states with a significance level of 0.01. A two-tailed test was adopted for testing mean and a one-tail test for pulsatility with the alternative hypothesis that pulsatility increased after closing box.

Table 2. A summary of mean heart rate for each of the five experiments at both box states, open (O) and closed (C), and the ARX model orders that were obtained by applying the MDL criterion.

Table 3. A comparison between the compliance value at the mean heart rate assessed using the apparent compliance approach $\left|C_{app}(\omega_{hr})\right|$ and a time domain pulse compliance approach C_{pulse}. Standard deviation of $\left|C_{app}(\omega_{hr})\right|$ was calculated using Eq.(10) and that of C_{pulse} was calculated by pooling all the beats for a given case.

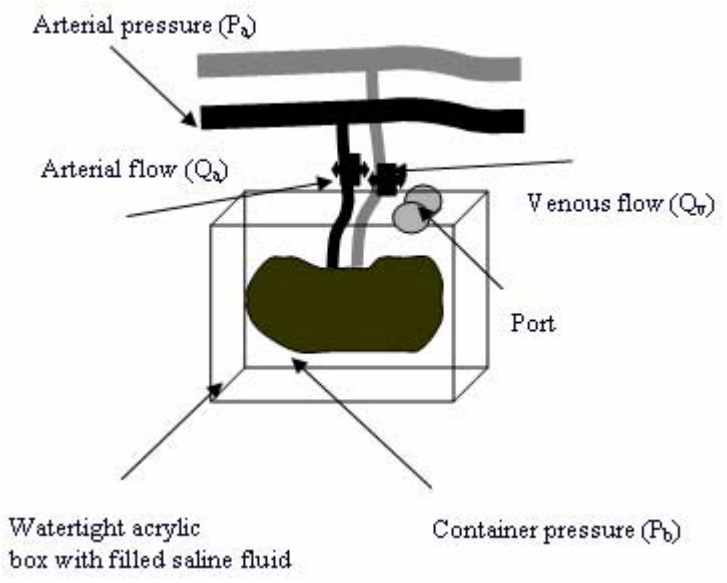
Arterial pressure (P_a)
Arterial flow (Q_a)
Venous flow (Q_v)
Port
Watertight acrylic
box with filled saline fluid
Container pressure (P_b)

Figure 1.

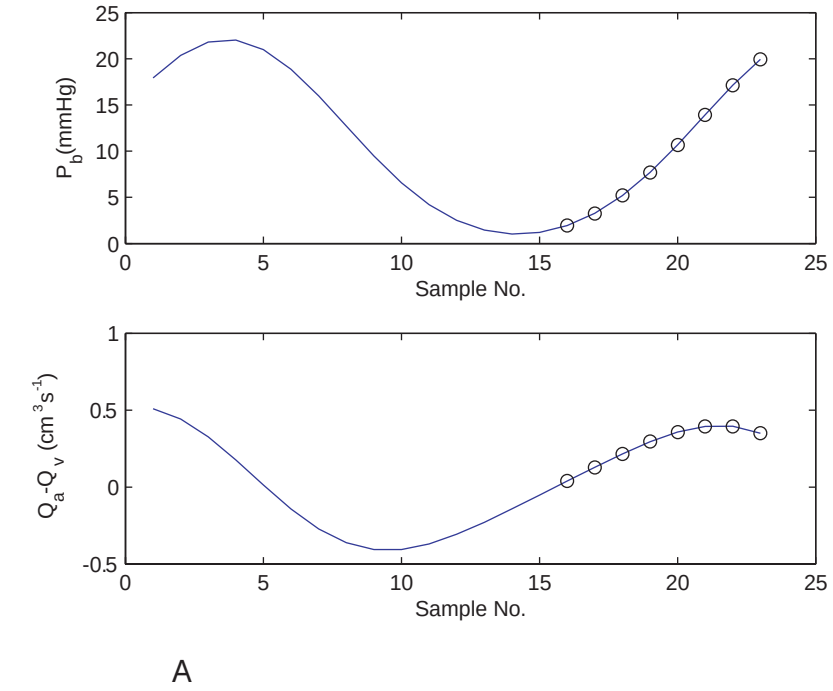
25
20
15
10
5
0
P_b(mmHg)
0
5
10
15
20
25
Sample No.
1
0.5
0
-0.5
Q_a-Q_v (cm^3s^{-1})
0
5
10
15
20
25
Sample No.

A

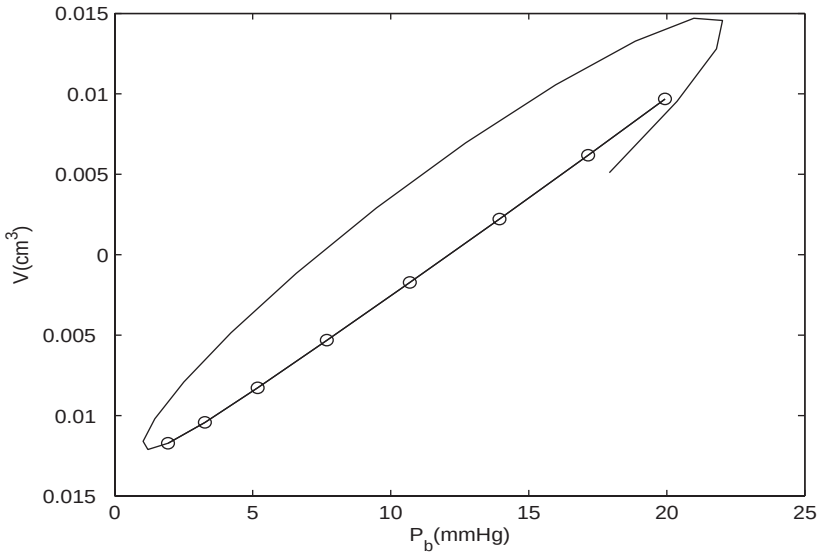
0.015
0.01
0.005
0
0.005
0.01
0.015
V(cm^3)
0
5
10
15
20
25
P_b(mmHg)

B

Figure 2.

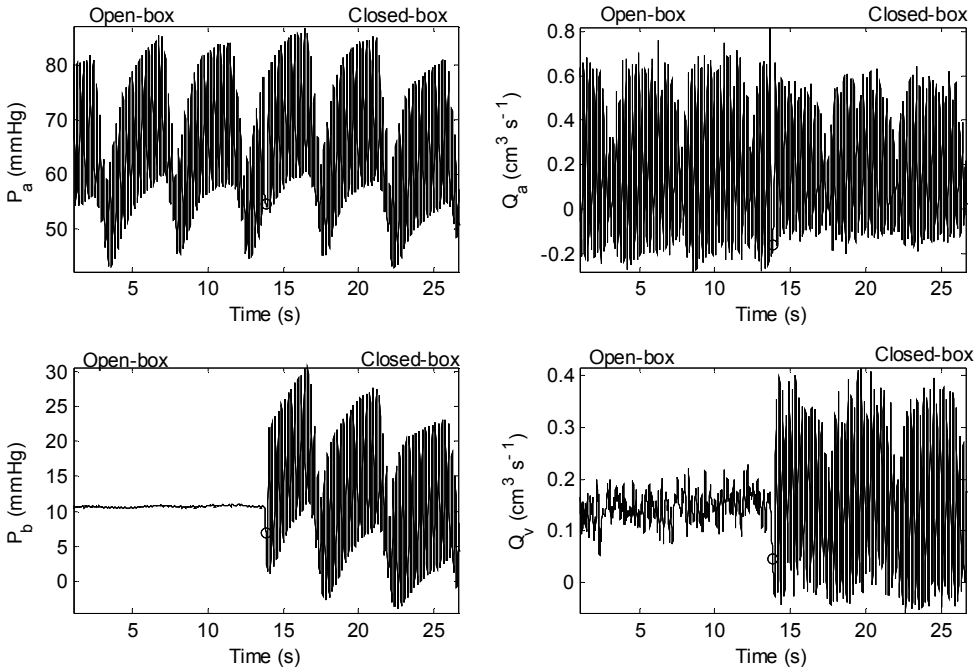

Figure 3.

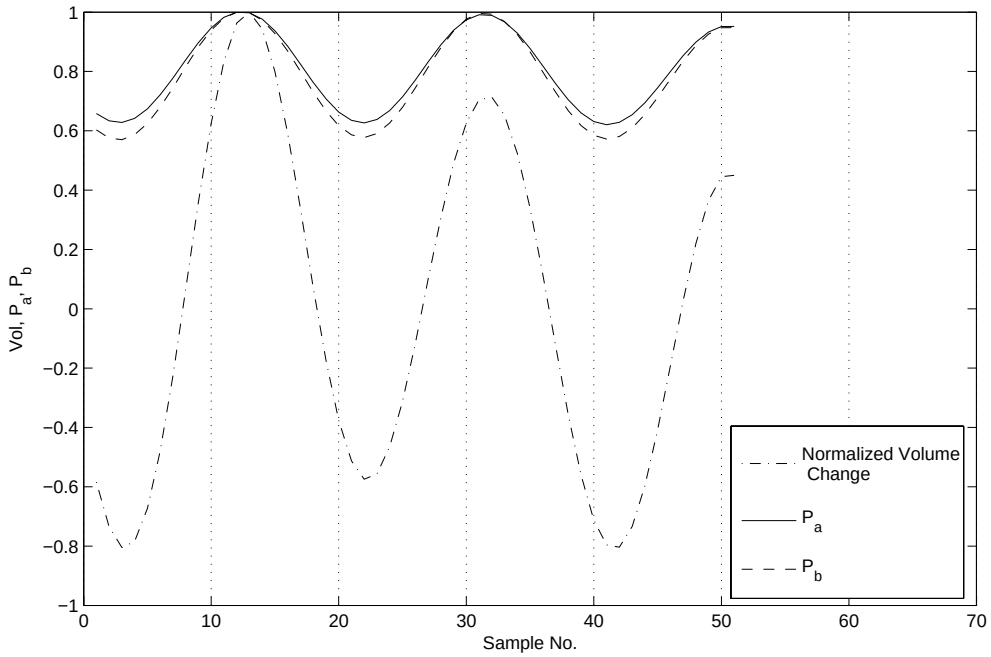

Figure 4.

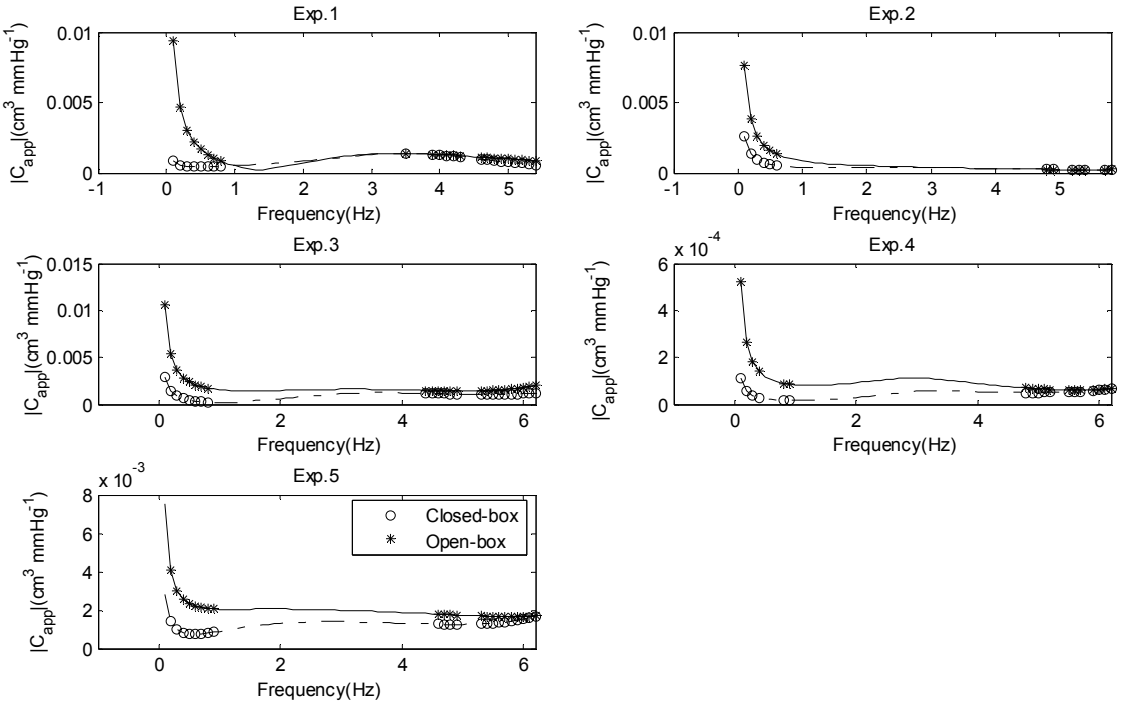
Exp.1
Exp.2
Exp.3
Exp.4
Exp.5
$|C_{app}|(cm^3\ mmHg^{-1})$
Frequency(Hz)
x 10^-3
x 10^-4
Closed-box
Open-box

Figure 5.

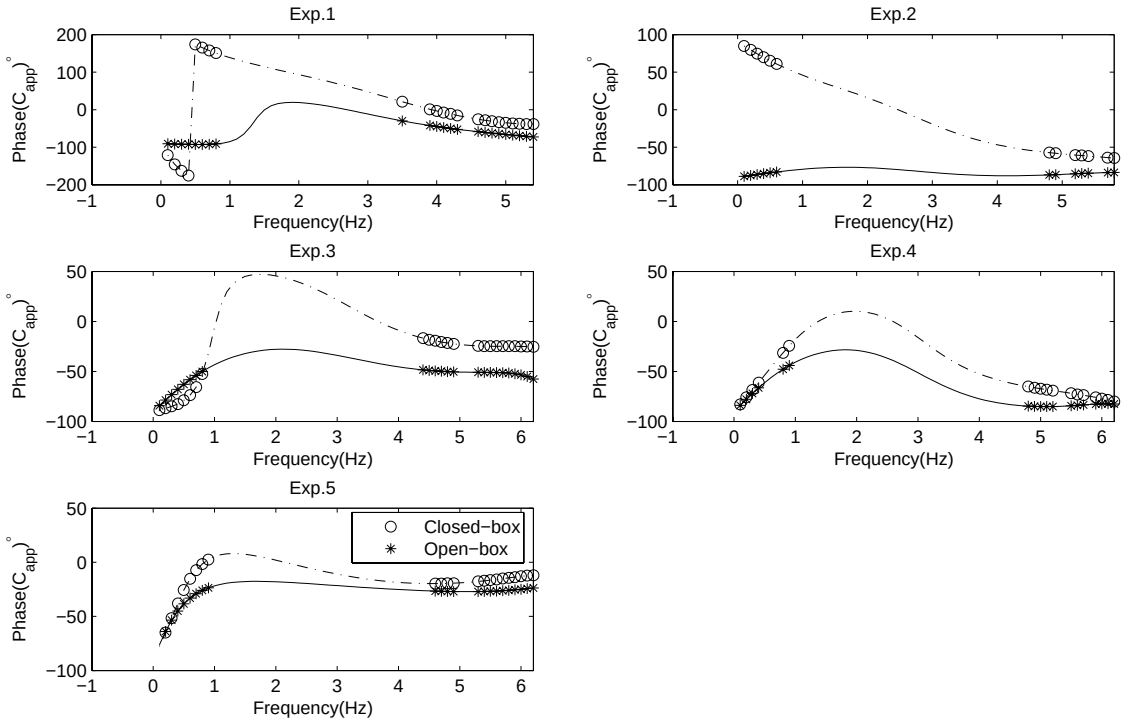
Exp.1
Exp.2
Exp.3
Exp.4
Exp.5
Phase(C_{app})°
Frequency(Hz)
Closed−box
Open−box

Figure 6.

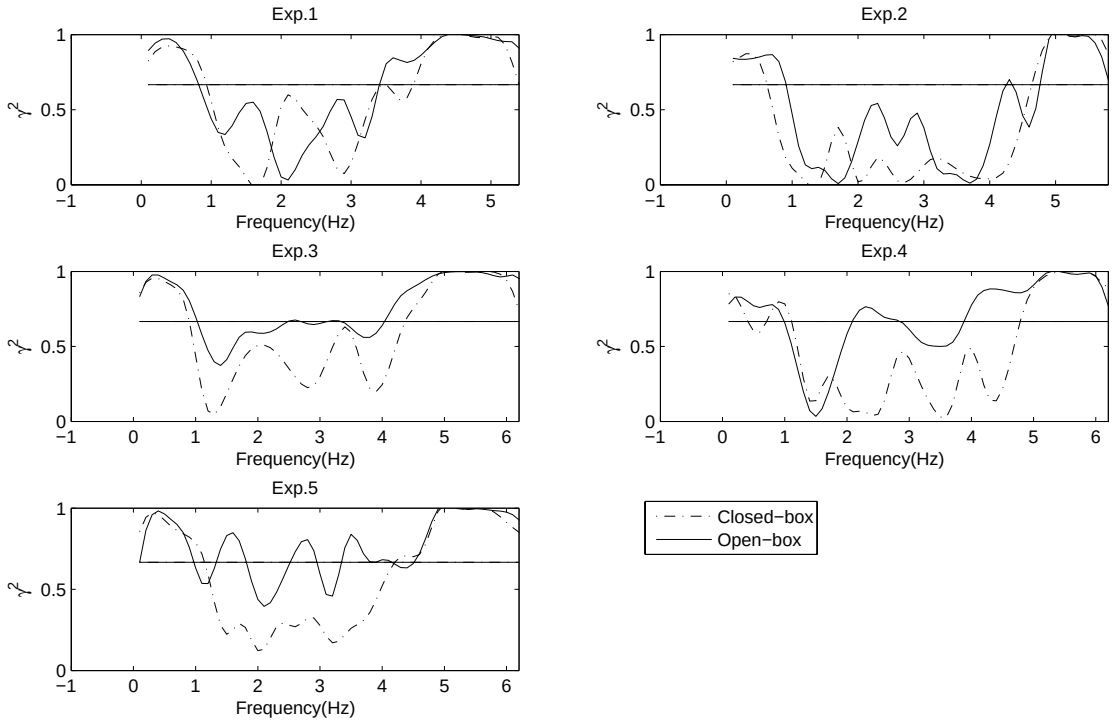
Exp.1
Exp.2
Exp.3
Exp.4
Exp.5
γ^2
Frequency(Hz)
Closed−box
Open−box

Figure 7.

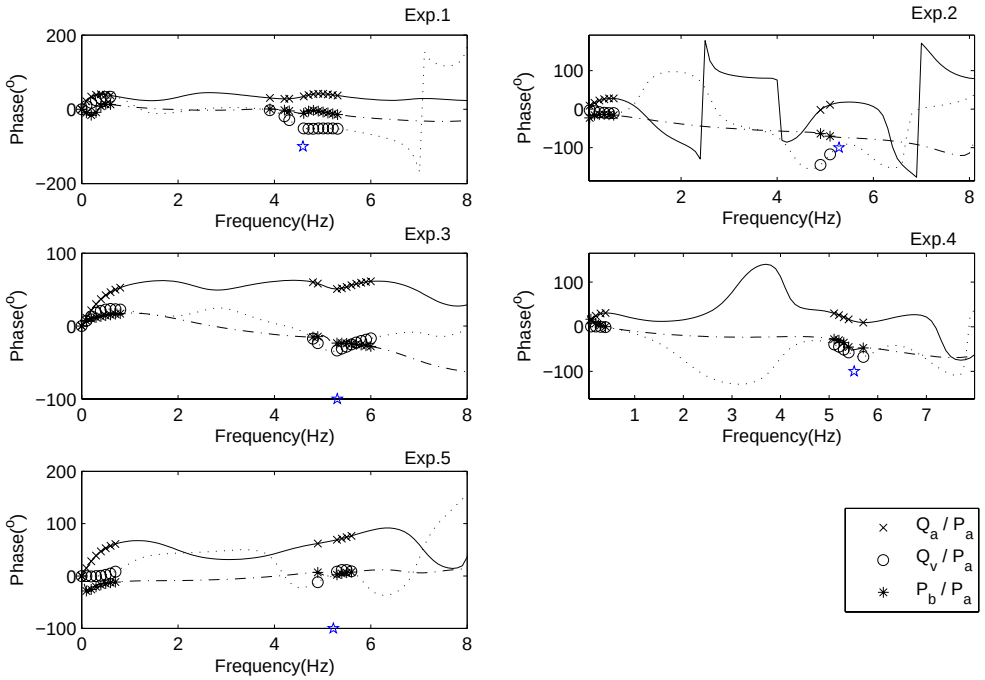

Figure 8.

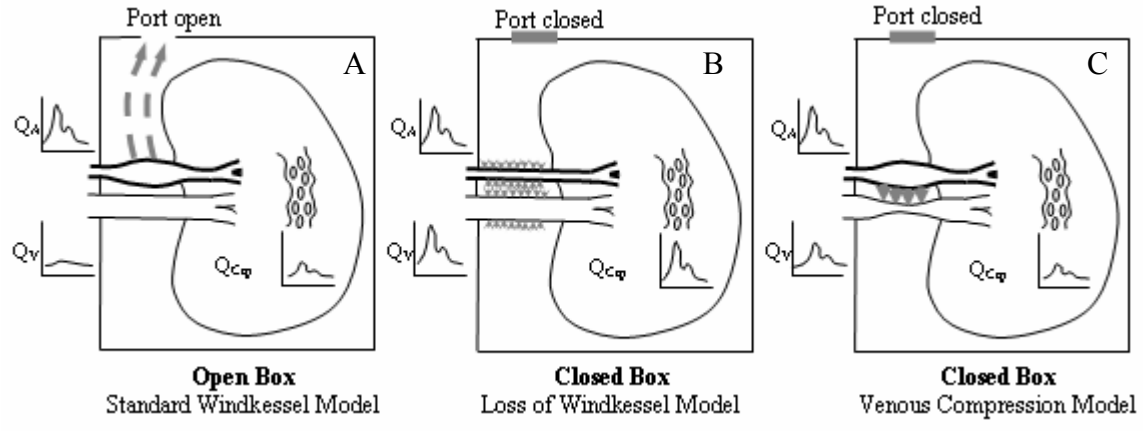
Port open
A
Port closed
B
Port closed
C
Q_A
Q_V
Q_{cap}
Open Box
Standard Windkessel Model
Closed Box
Loss of Windkessel Model
Closed Box
Venous Compression Model

Figure 9.

Table 1.

Exp.		P_a ± SD		Q_a ± SD		P_b ± SD		Q_v ± SD	
		M (mmHg)	P	M (cm^3s^{-1})	P	M (mmHg)	P	M (cm^3s^{-1})	P
1	C	65.397 ± 6.073	25.683 ± 3.659	0.209 ± 0.031	0.645 ± 0.115	12.486 ± 4.331 *	20.225 ± 2.519 *	0.158 ± 0.032	0.338 ± 0.053 *
	O	65.167 ± 5.519	24.704 ± 3.588	0.216 ± 0.036	0.825 ± 0.136	10.675 ± 0.106	0.135 ± 0.069	0.150 ± 0.016	0.051 ± 0.026
2	C	64.744 ± 3.724	31.485 ± 3.360	0.123 ± 0.014	0.222 ± 0.032	16.144 ± 3.836 *	16.435 ± 1.390 *	0.165 ± 0.016 *	0.063 ± 0.028 *
	O	65.396 ± 4.490	32.925 ± 3.579	0.128 ± 0.022	0.249 ± 0.032	9.328 ± 0.131	0.106 ± 0.047	0.177 ± 0.012	0.036 ± 0.020
3	C	68.685 ± 5.145	26.115 ± 3.319 *	0.241 ± 0.040	0.862 ± 0.162	9.103 ± 2.113 *	27.322 ± 4.139 *	0.121 ± 0.021	0.221 ± 0.049 *
	O	66.636 ± 4.893	23.909 ± 3.409	0.239 ± 0.035	1.136 ± 0.141	6.567 ± 0.091	0.302 ± 0.094	0.122 ± 0.011	0.034 ± 0.019
4	C	61.556 ± 3.834 *	26.888 ± 3.928	0.012 ± 0.002	0.050 ± 0.007	9.662 ± 2.537 *	16.314 ± 1.875 *	0.022 ± 0.001 *	0.004 ± 0.002 *
	O	64.336 ± 3.807	27.085 ± 3.389	0.012 ± 0.003	0.058 ± 0.008	11.831 ± 0.116	0.117 ± 0.058	0.021 ± 0.001	0.002 ± 0.001
5	C	65.451 ± 4.218	29.701 ± 3.981 *	0.300 ± 0.096 *	1.164 ± 0.342	17.911 ± 3.597 *	10.980 ± 1.130 *	0.179 ± 0.046	0.101 ± 0.038 *
	O	64.020 ± 3.449	25.897 ± 2.987	0.358 ± 0.082	1.355 ± 0.278	14.467 ± 0.483	6.568 ± 1.398	0.190 ± 0.033	0.055 ± 0.028

Table 2.

Exp.	HR ± SD (Hz)		N_u (AR model order)		N_y (AR model order)	
	O	**C**	**O**	**C**	**O**	**C**
1	4.60 ± 0.11	4.60 ± 0.11	6	6	8	8
2	5.24 ± 0.12	5.27 ± 0.11	6	6	5	5
3	5.29 ± 0.13	5.29 ± 0.14	6	6	7	7
4	5.37 ± 0.33	5.50 ± 0.13	6	6	8	4
5	5.27 ± 0.12	5.22 ± 0.10	6	6	6	8

Table 3.

Exp.	$\left\|C_{app}(\omega_{hr})\right\|$ (10^{-3} cm^3 mmHg^{-1})	C_{pulse} (10^{-3} cm^3 mmHg^{-1})	$\left\|C_{app}(\omega_{hr})\right\| / C_{pulse}$
1	0.977 ± 3.772	1.210 ± 0.168	0.807
2	0.239 ± 1.912	0.514 ± 0.158	0.465
3	1.057 ± 2.643	1.051 ± 0.105	1.006
4	0.052 ± 0.651	0.076 ± 0.009	0.684
5	1.280 ± 2.790	3.412 ± 0.451	0.375